Biophysical Journal, Volume 99

Supporting Material

The shear-stabilized rolling behavior of E. coli examined with simulations

Matthew Whitfield, Tia Ghose, and Wendy Thomas

Measurement of Bond Parameters

The parameters for the two-state, allosteric catch bond model used in the paper were estimated individually from experiments or crystal structure data that best probed each parameter as described below.

Single Molecule Atomic Force Microscopy.

k_{20}^0 and x_{20} were determined with high accuracy in AFM experiments by Yakovenko et al. (1). In that paper, the K12 variant of FimH, when bound to mannose-BSA and pulled at constant velocity, demonstrated catch bond behavior with two distinct peaks in the histogram of the rupture forces. Histograms at three different loading rates were simultaneously fit with the two-state, allosteric catch bond model generating estimates of 5.1×10^{-6} s^{-1} for k_{20}^0 and 4.52 A for x_{20}. The other 6 parameters of the model were not well determined in that experiment, since together they were determined by just 5 or 6 data points in the low-force peak that is lost at higher pulling velocities. However, k_{20}^0 and x_{20} are well-estimated, as they alone determine the location of the high-force peak over a range of pulling velocities. Moreover, a high-affinity variant of FimH (A188D) showed classic slip bond behavior consistent with the two-parameter slip bond model using the identical values of k_{20}^0 and x_{20}. Together, this indicates that these values of k_{20}^0 and x_{20} are well estimated and are appropriate for a wide range of FimH variants, so we use them here for KB-91 FimH.

Justification for using the 8-parameter catch bond model.

As noted above, the remaining 6 parameters were not well estimated in single molecule AFM experiments since the allosteric catch bond model overfits the data. However, simpler models were insufficient to explain the data (1), since the slip bond model (2) could not reproduce the loss of the low-force peak at higher loading rates, while other catch bond models with either 4 or 5 parameters (3, 4) cannot explain the history dependence reported in Figure 5 of Yakovenko et al. (1). The 6 parameters are also not well estimated from fitting the allosteric catch bond model to the pause lifetimes of bacteria binding in flow (5), since that experiment contains all the complex cell mechanics addressed in this manuscript, which are not accounted for in the model for bond mechanics. We therefore attempted to measure the remaining parameters with increased accuracy where possible, or determine that they were not critical to the behavior probed in our simulations when they could not be directly measured.

Microbead flow chamber experiments.

Mannose-BSA-coated 2.7 μm diameter polystyrene microspheres (Polysciences, Inc) were bound to a surface coated with KB-91 FimH in the form of fimbrial tips (purified as described previously (6)). The microspheres were introduced into the flow chamber at a high shear rate (0.27 Pa) which produced an estimated drag force on the bead of 16 pN and even higher forces on the bond due to the lever arm effect. Beads bound in a stationary manner in these conditions suggesting that bonds had transitioned into state 2, consistent with the long-lived bonds observed in single molecule AFM experiments at high forces (6). Four percent soluble alpha-methyl-mannopyranoside (SIGMA) was added to inhibit the formation of new bonds, and then the flow rate was dropped to a low shear (0.0033 Pa) with an estimated drag force of just 0.2 pN. This allowed us to observe the fate of state 2 bonds in near-equilibrium conditions. The beads were tracked until they began moving again and the initial stages of the survival plot of the fraction of beads remaining over time was fit with a single exponential to obtain a time constant of 0.025 s^{-1}.

This was done in the presence of soluble mannose preventing new bond formation. In addition, stationary adhesion lasted much longer than expected simple from multiple bonds as bond lifetimes only increase logarithmically with bond number if new bonds cannot form (7). Based on these factors, it can be concluded that multiple short-lived bonds were not mediating the stationary behavior. We hypothesized that this time constant corresponded to bonds breaking at low force as they revert to state 1 (k_{21}^0) and then rapidly unbind rather than mannose directly unbinding from FimH while it is in state 2 (k_{20}^0). If this is the case, then increasing the bond force (by increasing shear stress) should increase the time it takes for beads to detach, by preventing reversion to state 1. Indeed, in experiments where the shear stress was switched to a higher shear stress than 0.0033 Pa (from 0.1 - 0.52 Pa), very few beads detached even after 5 minutes, and the estimated time constant increased over 25-fold. We thus assigned k_{21}^0 = 0.025 s^{-1}. Because of the uncertainty of the amount of force in these experiments, they cannot be used to estimate the force sensitivity of this transition (x_{21}). Also, the time resolution is not sufficiently high to measure the low-affinity lifetime. We thus turned next to other methods for these parameter measurements.

Surface Plasmon Resonance Experiments.
To determine what happens to the low-affinity state in the absence of force, KB-91 fimbrial tips were injected over a mannose-BSA coated chip in a BioCore 2000® Surface Plasmon Resonance instrument as described previously (6). When the response reached an equilibrium value (after 2 minutes), the tips were washed out. Within 1 second, the time resolution of the instrument, most of the tips had already detached, telling us that the detachment rate from state 1 without force (k_{10}^0) must be faster than 1 s^{-1} but not determining the precise value. For this reason, this parameter is varied in the paper to see whether the precise value is important to bacterial adhesive behavior. Only 5% of the signal present at equilibrium before the wash remained after 1 second. This fraction exhibited a slow decay suggesting that, at equilibrium, 5% of the bonds are in state 2, so that $k_{12}^0 = 0.05 * k_{21}^0$ resulting in the k_{12}^0 = 0.00125 s^{-1} estimate used in this paper.

Crystal structure analysis.
We currently lack methods to determine the force sensitivity of most of the bond transitions, since this requires a method that has high force resolution at low forces (unlike the AFM), provides for accurate calibration of the forces (unlike the flow chamber microsphere experiments), and is stable for long enough time periods to accurately measure very slow transitions (unlike the AFM and optical tweezers). In this way, the complexity and long lifetimes of the two-state FimH system provides challenges not previously encountered in parameterizing other receptor-ligand interactions. We thus take an alternative approach to the force sensitivity, which is to evaluate the crystal structure to determine the transition state distances x_{ij}, which in turn determine the force sensitivity since rates increase exponentially with $f * x_{ij}/(k_B T)$. First, we found that the mannose-binding pocket of the low-affinity FimH crystal structure is essentially identical to that of the high-affinity structure (6), differing only in that one side was more open in the low-affinity state, allowing rapid binding and unbinding. Moreover, in molecular dynamic simulations (unpublished results), it was observed that mannose docked into this structure unbound from the pocket through a similar pathway as the high affinity state. This suggests that the transition states in the two systems are similar, and so we used the same value for x_{10} as for x_{20}.

Next, we considered the elongation that occurs between the low-affinity and high-affinity crystallized states. FimH has a hooked structure than hinges at residue 160 (hereafter called the hinge point), creating an angle of 135° between the mannose-binding lectin domain of FimH and the pilin domain that anchors FimH to the fimbriae by accepting a donated beta strand from the next subunit, FimG {P. Aprikian, G. Interlandi, B. Kidd, I. Le Trong, V. Tchesnokova, O. Yakovenko, E. Bullitt, R. E. Stenkamp, W. E. Thomas, and E. V. Sokurenko, under review}. However, the two domains are hypothesized to unhinge and straighten when force is applied, and indeed this is observed in steered molecular dynamics simulations in the Aprikian paper. This force-induced straightening eliminates most of the contacts between the lectin and pilin domains. These contacts maintain the lectin domain in the low-affinity state, so that loss of the contacts would allow the lectin domain to switch to the high-affinity state. We thus assume that the transition state between the low-affinity and high-affinity state is at the point where FimH has opened the hinge angle, because, at this point, the angle might close again or the structure might undergo further conformational changes. We thus calculate the distances involved in reaching this transition, which is the hinge opening for x_{12} and the conformational switch from high-affinity to low-affinity for x_{21}. Analysis of the 2JWN crystal structure deposited in the protein database (6) reveals that FimH is 73 A in length between residue 1 in the mannose-binding site (hereafter called simply the mannose binding site) and residue 13 of FimG, which can be considered the anchor point of FimH to the fimbriae and is thus hereafter called the anchor point. However, the lectin domain is 38 A in length between the mannose-binding site and the hinge point, while the pilin domain is 47 A from hinge point to the anchor point. When the hinge opens, FimH is thus expected to be 38 + 47 = 85 A from binding site to anchor point, for an elongation of 12 A, so that x_{12} = +12 A. Between the high-affinity (8) and low-affinity (6) states, the lectin domain compresses 12 A from the mannose site to the hinge point, so that x_{21} = -12 A. Note that the total difference in length is thus 24 A, and that it appears to be a coincidence that this length is evenly split at the transition point.

Fimbrial forces exerted on the cell

In our model, fimbriae transmit forces to the cell through both axial tension and compression and deviations from their orthogonal projection. Fig. S1 shows a 2D representation of the modeled forces from a single fimbriae acting on the cell. The tensile or compressive force F_b that arises when a fimbriae is bound, and thus constrained at its tip, is $k_a * \Delta L$ where k_a is the axial spring constant and ΔL any deviation from equilibrium fimbrial length. The tips of unbound fimbriae that contact the surface are assumed to have no friction with the surface and thus slide along the surface keeping their equilibrium length while producing no axial forces. The force normal to the fimbriae F_α that arises when it is bent away from orthogonal is $\alpha * k_t$/L where α is the angle between the fimbriae and orthogonal and k_t is the torsional spring constant of that fimbriae. The torque on the cell is found by calculating the moment that these forces create around the center of the cell. The total translational force on the cell in each direction is found by resolving these forces into the x, y, and z directions and summing for all fimbriae contacting the surface.

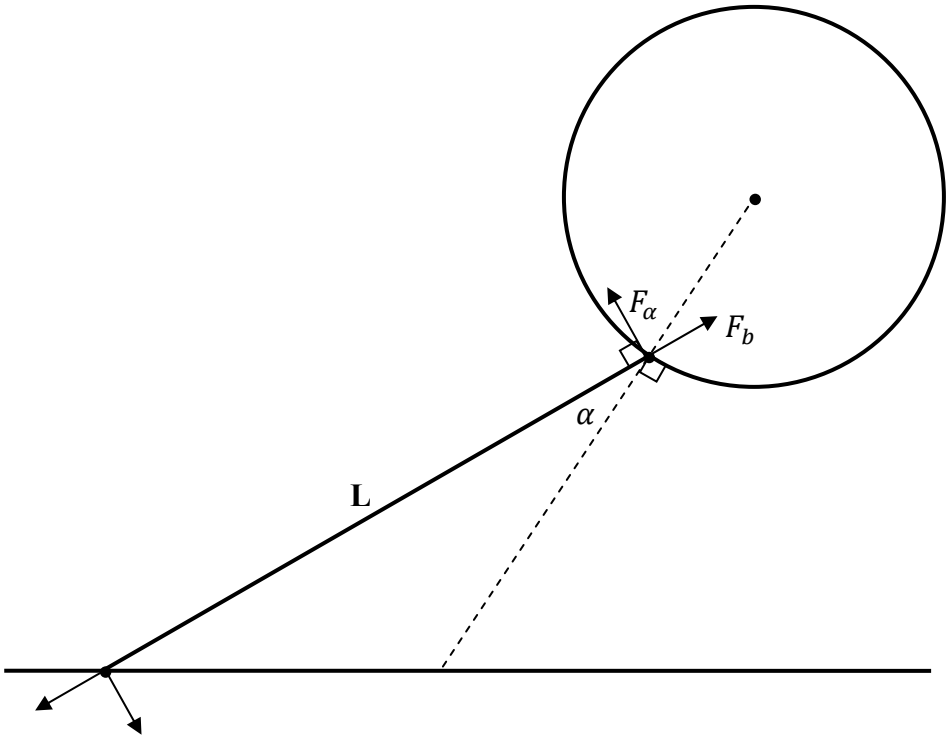

FIGURE S1. Schematic of the forces imparted to the cell by a single fimbriae.

Ermak algorithm

The movement and rotation of the cell is controlled using the damping algorithm derived by Ermak (9, 10). The algorithm allows for the accurate simulation of movements independent of the relationship between the time step and diffusive relaxation rates of the proteins and cell. The algorithm essentially serves to dampen movements with frictional coefficients that are a function of the time step and drag coefficient of the cell. In the case of translation, the diffusive relaxation rate ξ_{trans} is γ/m where $\gamma = 6\pi\eta r_{drag}$, $m = 4\pi\eta r_{cell}^3/3$, and r_{drag} is the effective drag radius (neglecting the fimbriae in the mass calculation). Because the cell is surrounded by fimbriae, the mean fimbrial length is added to the radius of the cell for the purposes of calculating the drag on the cell. Analogously for rotation: $\xi_{rot} = \gamma/I$ where $\gamma = 8\pi\eta r_{drag}^3$ and $I = 2mr_{drag}^2/5$. The frictional coefficients are

$c_o = e^{-\xi\Delta t}$, $c_1 = \frac{1-c_o}{\xi\Delta t}$, and $c_2 = \frac{1-c_1}{\xi\Delta t}$ for translation and

$c_{orot} = e^{-\xi_{rot}\Delta t}$, $c_{1rot} = \frac{1-c_o}{\xi_{rot}\Delta t}$, and $c_{2rot} = \frac{1-c_1}{\xi_{rot}\Delta t}$ for rotation.

The tensions (F) and torques (τ) from each fimbriae are calculated as previously described in each time step and summed to determine the translational (a) and angular (α) accelerations of the cell: $a_x = F_x/m$, $a_y = F_y/m$, and $a_z = F_z/m$ for translation and $\alpha_x = \tau/I$, $\alpha_y = \tau/I$, and $\alpha_z = (\tau + \tau_s)/I$

for rotation where τ_s is the shear rotational contribution from the fluid (11, 12). Translational (v) and angular (ω) velocities are then calculated:

$$v_x = c_o(v_{xo} - \upsilon) + c_1 a_x \Delta t + \upsilon$$

$$v_y = c_o v_{yo} + c_1 a_y \Delta t$$

$$v_z = c_o v_{zo} + c_1 a_z \Delta t$$

$$\omega_i = c_o \omega_{io} + c_1 \alpha_i \Delta t$$

where υ is the fluid velocity and i is x, y, or z. The translation of the cell can then be determined:

$$x = x_o + c_1(v_x - \upsilon)\Delta t + c_2 a_x \Delta t^2 + \upsilon \Delta t$$

$$y = y_o + c_1 v_y \Delta t + c_2 a_y \Delta t^2$$

$$z = z_o + c_1 v_z \Delta t + c_2 a_z \Delta t^2 .$$

The rotation of the cell is updated using the calculated angular velocities and Beard's method for unbiased 3D rotations(13).

Flow chamber experiments and data analysis

KB-91 *E. coli* were flowed over a mannose-coated 35 mm Corning tissue culture treated polystyrene dish at different shear rates while recording the cells' progression along the chamber with a 37 ms frame rate video lasting 10 s. Bacteria display a switch from mostly free floating, to rolling, to initiation of stationary behavior over the range of shear rates from 10 to 1000 s^{-1}, which is the range used for simulations. Cells that are stationary at the onset are excluded to match the conditions at the start of simulations.

To compare results between experiments and simulations, data points every 37 ms were considered in simulations in order to match the frame rate of experimental videos. Because a smoothing average of 4 points was necessary to eliminate noise in the experimental data, this was also employed when analyzing simulations. Cells are classified as free floating, rolling, or paused at each time point. Cells are considered free floating if the instantaneous velocity v is at least 50% of the hydrodynamic velocity, paused if v is less than 0.01% of the hydrodynamic velocity over 20 time steps, and rolling at v in between. If two rolling events are separated by a pause of less than 1 s then the cell is considered to be rolling during the whole event.

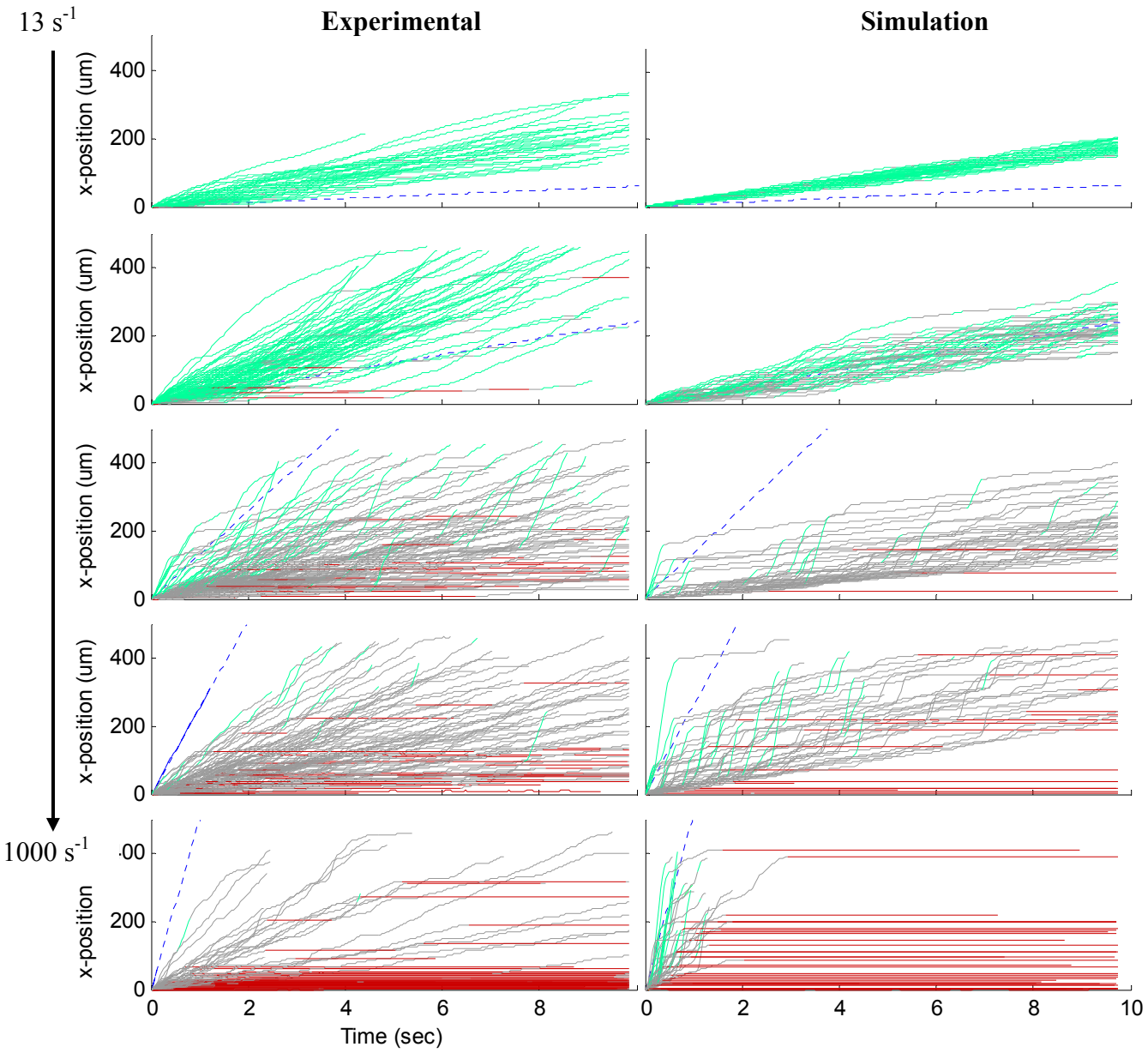

FIGURE S2 Comparison of experimental (*left*) and simulation (*right*) trajectories at shear rates from 13-1000 s^{-1} with $\boldsymbol{k_{10}^0}$=20 s^{-1} and $\boldsymbol{k_{01}^0}$=12 s^{-1}. Trajectories are teal when free floating, gray when rolling, and red when paused. The dotted blue line is the hydrodynamic velocity. At the second shear rate (49 s^{-1}), simulated cells show more attachments. Simulations, which always have the same number of fimbriae, exhibit less variability in rolling velocity than experimental data. At the highest shear rate simulated, rolling cells do not roll as stably as experimentally observed. Fimbrial uncoiling may play a limited role at this shear and will be assessed in future simulations.

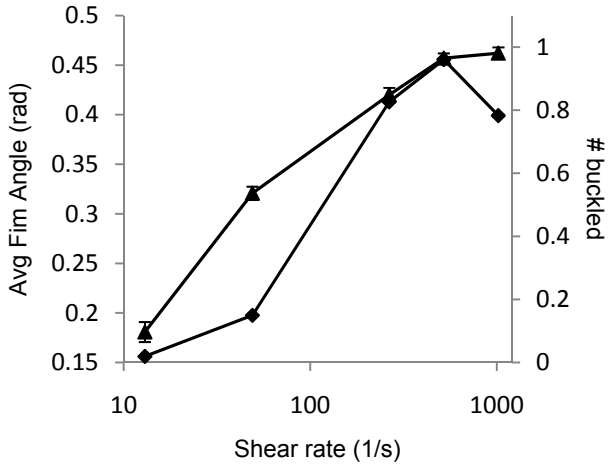

FIGURE S3 Fimbrial deflection (*triangles*) and buckling (*diamonds*) increase with shear in slip bond simulations. The slight decrease in the number buckled at the highest shear is due to the poor adherence of the cells at high shear when the catch bond transition is not allowed. Error bars are mean ± SE.

Supporting Movies

Simulated cells and their movement were visualized in Visual Molecular Dynamics (14) by treating the *E. coli* center (*royal blue*) and end points of the fimbriae as "atoms" and reconstructing fimbriae (*light blue*) as "bonds" between the two end points of each fimbriae. The y-plane origin represents the mannose-coated surface and is shaded gray. Fluid flow originating from the left side of the video drives the cells to the right. A green ball appears at the distal end of the fimbriae when a state 1 bond is formed and turns to red if the bond transitions into state 2. The ball turns yellow if the compressive force on the fimbriae causes it to buckle. Unbound fimbriae can be seen bending away from an orthogonal projection as they push against the surface. Videos show 200 ms of a representative trajectory at low, intermediate, and high shear. VMD is developed with NIH support by the Theoretical and Computational Biophysics group at the Beckman Institute, University of Illinois at Urbana-Champaign.

MOVIE S1 – Low shear showing only transient adhesions with little fimbrial deformation.
MOVIE S2 – Intermediate shear showing significant fimbrial deformation and sustained rolling behavior.
MOVIE S3 – High shear showing the transition to stationary adhesion with the conversion of one bond into state 2.

Previously published two-state, allosteric catch bond parameters for the FimH-mannose bond

The shear-enhanced phenomenon was roughly recreated with simulations using either the FimH-mannose bond parameters published in Thomas et al. (5) or Yakovenko et al. (1) obtained from fitting the two-state model to flow chamber and AFM data respectively. While the simulations qualitatively reproduced the experimental observations of shear-enhanced adhesion, they did not do so quantitatively, as demonstrated in Fig. S4. The quantitative differences are not surprising given the interdependence of the parameters due to globally fitting a single set of data and the

limitations inherent in each of the parameter fits (see Measurement of Bond parameters section above).

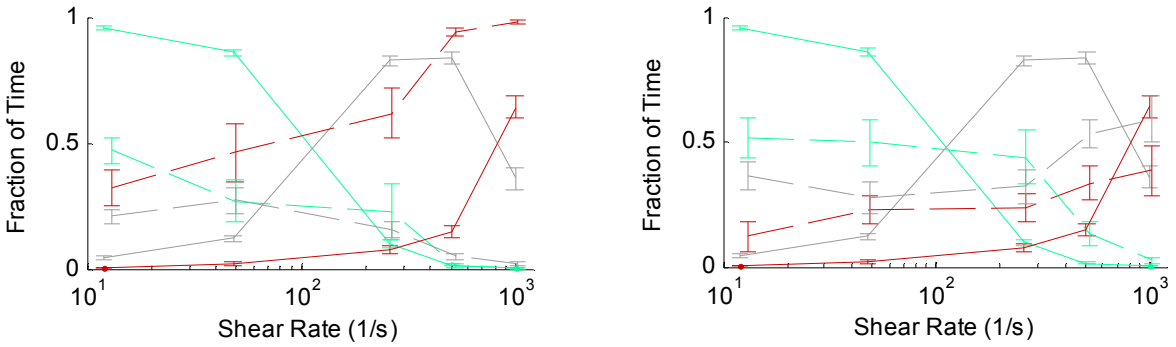

FIGURE S4 Comparison of previous parameter fits to experimental data. *A)* The average fraction of time that cells spend in each state (*teal=free floating, gray=rolling, red=stationary*) at was calculated at shear rates from 13-1000 s^{-1} for both experimental (*solid*) and simulation data (*dashed*) using parameters from Thomas *et al.* (5) with a k_{01}^0 of 2 s^{-1}. *B)* Same as *A* but simulations used parameters from Yakovenko *et al.* (1) with a k_{01}^0 of 0.5 s^{-1}. Error bars are mean ± SE.

1. Yakovenko, O., S. Sharma, M. Forero, V. Tchesnokova, P. Aprikian, B. Kidd, A. Mach, V. Vogel, E. Sokurenko, and W. Thomas. 2008. Fimh forms catch bonds that are enhanced by mechanical force due to allosteric regulation. J Biol Chem 283:11596-11605.
2. Evans, E., and K. Ritchie. 1997. Dynamic strength of molecular adhesion bonds. Biophys J 72:1541-1555.
3. Evans, E., A. Leung, V. Heinrich, and C. Zhu. 2004. Mechanical switching and coupling between two dissociation pathways in a P-selectin adhesion bond. PNAS 101:11281-11286.
4. Pereverzev, Y., O. V. Prezhdo, M. Forero, E. Sokurenko, and W. Thomas. 2005. The Two-Pathway Model for the Catch-Slip Transition in Biological Adhesion. Biophys J 89:1446-1454.
5. Thomas, W., M. Forero, O. Yakovenko, L. Nilsson, P. Vicini, E. Sokurenko, and V. Vogel. 2006. Catch-Bond Model Derived from Allostery Explains Force-Activated Bacterial Adhesion. Biophys. J. 90:753-764.
6. Le Trong, I., P. Aprikian, B. A. Kidd, M. Forero-Shelton, V. Tchesnokova, P. Rajagopal, V. Rodriguez, G. Interlandi, R. Klevit, V. Vogel, R. E. Stenkamp, E. V. Sokurenko, and W. E. Thomas. 2010. Structural basis for mechanical force regulation of the adhesin FimH via finger trap-like beta sheet twisting. Cell 141:645-655.
7. Tees, D. F. J., J. T. Woodward, and D. A. Hammer. 2001. Reliability theory for receptor-ligand bond dissociation. Journal of Chemical Physics 114:7483-7496.
8. Hung, C. S., J. Bouckaert, D. Hung, J. Pinkner, C. Widberg, A. DeFusco, C. G. Auguste, R. Strouse, S. Langermann, G. Waksman, and S. J. Hultgren. 2002. Structural basis of tropism of Escherichia coli to the bladder during urinary tract infection. Mol Microbiol 44:903-915.

9. Ermak, D. L., and J. A. McCammon. 1978. Brownian dynamics with hydrodynamic interactions. The Journal of Chemical Physics 69:1352.
10. Allen, M. P., and D. J. Tildesley. 1989. Computer simulation of liquids. Oxford University Press, USA.
11. Goldman, A., R. Cox, and H. Brenner. 1967. Slow viscous motion of a sphere parallel to a plane wall. II. Couette flow. Chem. Eng. Sci 22:653-660.
12. Goldman, A., R. Cox, and H. Brenner. 1967. Slow viscous motion of a sphere parallel to a plane wall. I. Motion through a quiescent fluid. Chem. Eng. Sci 22:637–651.
13. Beard, D. A., and T. Schlick. 2003. Unbiased rotational moves for rigid-body dynamics. Biophys J 85:2973-2976.
14. Humphrey, W., A. Dalke, and K. Schulten. 1996. VMD: visual molecular dynamics. J Mol Graph 14:33-38, 27-38.